

Ionospheric energy input as a function of solar wind parameters: global MHD simulation results

M. Palmroth¹, P. Janhunen¹, T. I. Pulkkinen¹, and H. E. J. Koskinen^{2,1}

¹Finnish Meteorological Institute, Geophysical Research Division

²University of Helsinki, Department of Physical Sciences

Manuscript submitted to

AG

Manuscript version from 17 December, 2002

Offset requests to:

M. Palmroth
FMI/GEO, P.O. Box 503
00101 Helsinki, Finland

Send proofs to:

M. Palmroth
FMI/GEO, P.O. Box 503
00101 Helsinki, Finland

Abstract

We examine the global energetics the solar wind magnetosphere ionosphere system by using the global MHD simulation code GUMICS-4. We show simulation results for a major magnetospheric storm (April 6, 2000) and a moderate substorm (August 15, 2001). The ionospheric dissipation is investigated by determining the Joule heating and precipitation powers in the simulation during the two events. The ionospheric dissipation is concentrated largely on the dayside cusp region during the main phase of the storm period, whereas the nightside oval dominates the ionospheric dissipation during the substorm event. The temporal variations of the precipitation power during the two events are shown to correlate well with commonly used AE-based proxy of the precipitation power. The temporal variation of the Joule heating power during the substorm event is well-correlated with a commonly used AE-based empirical proxy, whereas during the storm period the simulated Joule heating is different from the empirical proxy. Finally, we present a power law formula, which gives the total ionospheric dissipation from the solar wind density, velocity and magnetic field z -component and which agrees with the simulation result with more than 80% correlation.

1 Introduction

The energy transfer process between the solar wind and the magnetosphere and further between the ionosphere is one of the key questions in space physics, frequently brought up in executive summaries of many proposals and space physics research strategy reports (e.g., Acuña et al., 1995). While the energy transfer process was qualitatively explained already in the 1960's by the first theories of the solar wind - magnetosphere coupling (Dungey, 1961; Axford and Hines, 1961), the quantitative assessment of the problem has proven to be difficult. The energy transfer mechanism by which the solar wind energy enters the magnetosphere has been explained by magnetic reconnection and viscous interaction. The amount of transferred energy is still uncertain, because the results rely on correlations of solar wind parameters with known dissipation channels inside the magnetosphere (e.g., Akasofu, 1981). The first quantitative attempt using a global MHD simulation to identify both the amount of energy transferred through the magnetopause as well as the energy transfer locations at the magnetopause was made by Palmroth et al. (2003). They found that during southward interplanetary magnetic field (IMF) the locations of energy transfer are not only controlled by the locations where reconnection is likely to occur, but also by the focusing of the Poynting vector in the plane of the IMF clock angle (see also Papadopoulos et al., 1999). On the other hand, during northward IMF the Poynting flux focusing does not play a major role in determining the energy transfer locations, as reconnection may not have opened the magnetopause at the locations where the Poynting flux focuses (Palmroth et al., 2003).

The dissipation of the solar wind energy, both during magnetospheric substorms and magnetic storms, in the various sinks in the magnetosphere and the ionosphere has also been a subject of several older and more recent studies (Akasofu, 1981; Weiss et al., 1992; Lu et al., 1998; Turner et al., 2001; Pulkkinen et al., 2003). The understanding of the relative importance of the various sinks has changed over the years. For a long time the ring current was assumed to be the largest sink (Akasofu, 1981), whereas the more recent studies suggest that the polar ionosphere plays a major role in dissipating the solar wind energy (e.g., Weiss et al, 1992 and references therein). In the ionosphere the two largest dissipation mechanisms are the Ohmic Joule heating in the ionosphere when the field-aligned currents are closed across the equipotential surfaces, and the energy deposition by particles precipitating in the auroral region of the ionosphere.

The current understanding is that Joule heating consumes on the average more energy than particle precipitation (e.g., Lu et al., 1998), but the estimates for the relative importance of the particle precipitation have substantially increased from the 1% assumed originally (e.g., Akasofu, 1981).

At present, there are no direct ways to measure the energy deposited by Joule heating, only statistical estimates exist (e.g., Ahn et al., 1983) which give the amount of energy based on the ground magnetic variations caused by the auroral electrojets (such as the AE index). The AE index-based methods are only as good as the ability of the AE index to describe the temporal and spatial variations of the Pedersen currents not only within the auroral regions but in the polar cap as well. As the AE stations are located at high latitudes, the true intensity of the auroral electrojets is not recorded, particularly during major storms when the auroral oval moves significantly equatorward.

Measuring the energy deposited by particle precipitation is easier than measuring the energy deposited by Joule heating. When precipitating into the ionosphere, particles collide with atmospheric particles which emit auroral light that can be directly measured on the ground or from polar-orbiting satellites. A method based on ultraviolet image measurements onboard the Polar satellite was described by Østgaard et al. (2002). To generalize the results, they fitted the precipitation energy to the AL index, which then leads to similar problems related to the AE-based proxies as described above. The statistical distribution of electron precipitation can also be measured directly by polar-orbiting satellites. For example, Newell et al. (1996) found that the precipitation of auroral electrons is mainly centered in the 18-24 MLT sector. The latitudinal extent of the precipitation depends strongly on the level of magnetic variation: During large storms the oval moves equatorward, while during quiet times the auroral luminosity is concentrated on high latitudes.

There are only a few studies reporting on the energy deposition rate into the ionosphere using global models. Lu et al. (1998) were the first to apply the AMIE technique to estimate the energy deposition rate into the ionosphere during a magnetic storm. The AMIE procedure utilizes several models and a variety of measurements in an assimilative way. From the AMIE output Lu et al. (1998) derived the Joule heating and precipitation powers into the ionosphere and concluded that the temporal variation of the Joule heating and precipitation power resembled that of the AE index. Lu et al. (1998) determined the globally integrated average of Joule heating rate as 190 GW and the average precipitation power as about 90 GW during the storm.

The global MHD simulations can also be used to investigate the energy flow in the coupled solar wind - magnetosphere - ionosphere system. The recent development of the global MHD simulations has focused on the prediction of the magnetospheric state from a given solar wind input, while systematic examination of the magnetospheric response to given solar wind still awaits to be done. Several attempts along this direction have shown to be useful, particularly in cases where the parameters describing the solar wind - magnetosphere - ionosphere coupling are either difficult or impossible to measure globally. For example, the global MHD simulations have been used in

mapping the Poynting flux from the solar wind into the magnetosphere to examine the energy flow paths (e.g., Walker et al., 1993; Papadopoulos et al., 1999).

This paper is a continuation of the work by Palmroth et al. (2003) who developed a quantitative method to determine the energy transfer across the magnetopause in a global MHD simulation. Here we calculate the ionospheric energy dissipation, namely the Joule heating and precipitation powers, in the GUMICS-4 global MHD simulation. We determine the latitudinal and longitudinal distributions of the dissipated energy, as well as the temporal variation of the ionospheric dissipation. We analyze results from two simulated events, a magnetic storm that occurred on April 6-7, 2000, and a substorm that occurred on August 15, 2001. Our final aim is to develop a simple relationship between the solar wind input and ionospheric output. In Section 2 we introduce the GUMICS-4 global MHD simulation and the calculation of the ionospheric Joule heating and the precipitation powers; furthermore, we examine theoretically how the ionospheric output depends on solar wind parameters in ideal MHD. Section 3 describes the observations and the simulation results for the two events. In Section 4 we present the results, i.e., the calculated energy dissipation and the latitudinal and longitudinal dissipation distributions for the two events. In Section 4.4 we present the fit of the solar wind input data to calculated ionospheric output. Finally in Section 5 we summarize our results and end with discussion.

2 Model Description

2.1 GUMICS-4 Global MHD Simulation

GUMICS-4 (Janhunen, 1996) is a global 3-dimensional MHD simulation code that couples the solar wind - magnetosphere - ionosphere system in a simulation box with an automatically adaptive Cartesian octogrid. The GUMICS-4 simulation solves the fully conservative MHD equations in the solar wind - magnetosphere domain, whereas electrostatic equations are solved in the ionospheric domain. The simulation box reaches from $X_{GSE} = 32 R_E$ upwind to $X_{GSE} = -224 R_E$ in the antisunward direction, and in the Y_{GSE} and Z_{GSE} directions to $\pm 64 R_E$. The lower limit of the magnetospheric domain is a $3.7 R_E$ -radius spherical shell, from which the field-aligned currents and electron precipitation are mapped to the ionosphere using the dipole field. The electrostatic potential equation is solved in the ionosphere and mapped back to the inner boundary of the magnetosphere and used as a boundary condition for the MHD equations. The spherical ionosphere uses a triangular fixed grid, in which the oval region is more refined than e.g. the equatorial region. The simulations of the two events were carried out in a code setup similar to that described

in Palmroth et al. (2001). In the April 2000 storm simulation the smallest grid size was $0.5 R_E$, whereas the August 15, 2001, substorm simulation the smallest grid size was $0.25 R_E$. In the April 2000 storm simulation the IMF B_x was set to zero to ensure the divergence-free input magnetic field. In the August 15, 2001, substorm simulation the IMF B_x was set to a constant value of -3 nT, which corresponds to the observed value of IMF B_x before 5 UT. Consequently, the input magnetic field at the time of onset (~ 0430 UT) was modeled accurately. Of course, constant B_x fulfills the divergence-free condition.

2.2 Energy dissipated into the ionosphere

The ionospheric dissipation is calculated as a sum of the power consumed by Joule heating P_{JH} and the precipitating particles. The Joule heating power is calculated as

$$P_{JH} = \int \mathbf{E} \cdot \mathbf{J} dS = \int \Sigma_P E^2 dS, \quad (1)$$

where \mathbf{E} is the electric field, \mathbf{J} the current density, Σ_P the height-integrated Pedersen conductivity, and dS the area element on the spherical ionospheric surface. The quantities are interpolated from the simulation results in an ionospheric grid with a resolution of 1° in latitude and 3° in longitude.

The energy associated with particle precipitation is obtained using formulas given by Robinson et al. (1987), where the height-integrated ionospheric Pedersen and Hall conductivities Σ_P and Σ_H are calculated using the energy flux and the average energy of precipitating electrons. In the present study, we obtain the height-integrated conductivities from the simulation results and analytically invert equations (3) and (4) of Robinson et al. (1987) to get the precipitation energy flux.

2.3 Similarity scaling laws

Consider the ideal MHD equations written in the primitive variable form

$$\partial_t \rho = -\nabla \cdot (\rho \mathbf{v}) \quad (2)$$

$$\rho (\partial_t \rho + \mathbf{v} \cdot \nabla \rho) = -\nabla P + \mathbf{j} \times \mathbf{B} \quad (3)$$

$$\partial_t \mathbf{B} = \nabla \times (\mathbf{v} \times \mathbf{B}) \quad (4)$$

$$(\partial_t + \mathbf{v} \cdot \nabla) (P \rho^{-\gamma}) = 0. \quad (5)$$

where $\mathbf{j} = \nabla \times \mathbf{B} / \mu_0$. Furthermore, let us concentrate on stationary solutions ($\partial_t = 0$), and decompose $\mathbf{B} = \mathbf{B}_0 + \mathbf{B}_1$ where \mathbf{B}_0 is the Earth's internal field and \mathbf{B}_1 is the externally induced part.

Thus, any solution of Eqs. (2-5) is defined by four functions of three coordinates $\rho(\mathbf{x})$, $\mathbf{v}(\mathbf{x})$, $P(\mathbf{x})$ and $\mathbf{B}_1(\mathbf{x})$. The similarity scalings of such solutions are new solutions $\rho'(\mathbf{x})$, $\mathbf{v}'(\mathbf{x})$, $P'(\mathbf{x})$ and $\mathbf{B}'_1(\mathbf{x})$ which are related to the original ones by $\rho'(C_L\mathbf{x}) = C_\rho\rho(\mathbf{x})$, $\mathbf{v}'(C_L\mathbf{x}) = C_v\mathbf{v}(\mathbf{x})$, $P'(C_L\mathbf{x}) = C_P P(\mathbf{x})$ and $\mathbf{B}'_1(C_L\mathbf{x}) = C_{B_1}\mathbf{B}_1(\mathbf{x})$ where C_ρ , C_v , C_P and C_{B_1} are the scaling factors for density, velocity, pressure and perturbation magnetic field, and C_L is the scaling factor for spatial coordinates. We also introduce a scaling factor C_{B_0} for the internal magnetic field in the same way as for the dynamic variables, and require that the new functions satisfy Eqs. (2-5) with $\partial_t = 0$. In the stationary case, Eqs. (2) and (5) contain only one term and thus do not imply any conditions for the scaling factors, but the momentum equation (3) and Faraday's law (4) read

$$\rho\mathbf{v} \cdot \nabla\mathbf{v} - \frac{1}{\mu_0}(\nabla \times \mathbf{B}_1) \times \mathbf{B}_0 - \frac{1}{\mu_0}(\nabla \times \mathbf{B}_1) \times \mathbf{B}_1 + \nabla P = 0 \quad (6)$$

$$\nabla \times (\mathbf{v} \times \mathbf{B}_0) + \nabla \times (\mathbf{v} \times \mathbf{B}_1) = 0. \quad (7)$$

Applying the scalings and requiring that each possible pair of terms in Eqs. (6) and (7) scales in the same way we obtain the conditions

$$C_\rho C_v^2 = C_{B_1} C_{B_0} = C_{B_1}^2 = C_P, \quad (8)$$

i.e., $C_{B_0} = C_{B_1} = C_\rho^{1/2} C_v$, $C_P = C_\rho C_v^2$. Requiring that the internal field is the dipole field which scales as r^{-3} we obtain the connection $C_L = C_{B_0}^{-1/3}$ between the coordinate scaling C_L and the internal field scaling C_{B_0} . We thus see that C_ρ and C_v can be selected freely but the other scaling factors C_{B_1} , C_{B_0} , C_P and C_L follow from these two. In other words, by starting from a stationary solution which is valid for solar wind density ρ and velocity v , we obtain a two-parameter family of similarity solutions which spans all possible solar wind density and velocity combinations. The nature of the similarity solutions is such that if, e.g., the solar wind density is multiplied by 10, the density and pressure everywhere in the simulation box are also multiplied by 10, the magnetic fields by $\sqrt{10}$, and the spatial scales by $10^{-1/6} \approx 0.68$. The Earth therefore becomes larger relative to the magnetosphere if the solar wind density is increased, but otherwise the MHD solutions are self-similar. Apart from the changing ionospheric feedback and the inherent time-dependence of the solution, the similarity solutions should therefore correspond to what we obtain from GUMICS-4.

The ionospheric Joule heating is proportional to the square of the current flowing through the ionosphere, if the ionospheric conductivity pattern and the geometry of the current stay constant. The Joule heating P_{JH} is given by an ionospheric area integral $P_{\text{JH}} = \int dS J_P^2 / \Sigma_P$ where Σ_P is the height-integrated Pedersen conductivity and J_P is the height-integrated Pedersen current. The

MHD similarity solutions scale such that the polar cap expands or shrinks but the current pattern stays approximately self-similar. If the total current I flowing through the ionosphere is kept constant, J_P is proportional to I/R_{PC} where R_{PC} is the polar cap radius. Since the polar cap area is proportional to R_{PC}^2 , the Joule heating P_{JH} is independent of R_{PC} . Thus we conclude that, approximately, P_{JH} is proportional to I^2 . The total current I flowing through the ionosphere scales in the same way as the magnetospheric current systems, thus we obtain $I \sim jL^2$ where the current density $j \sim B_1/L$ and L is the spatial length, i.e. $I \sim (B_1/L)L^2 = B_1L \sim P^{1/2}P^{-1/6} = P^{1/3}$ where P is the solar wind dynamic pressure. Thus $P_{JH} \sim P^{2/3} \sim (\rho v^2)^{2/3} \sim \rho^{2/3}v^{4/3}$.

The ionospheric particle precipitation energy flux per unit area from a magnetospheric Maxwellian source plasma is proportional to $P_{th}v_{th}$ where P_{th} is the thermal pressure of the source plasma and $v_{th} \sim v$ its thermal velocity (Janhunen and Olsson, 1998). Thus the total power of particle precipitation P_{prec} scales as $P_{prec} \sim P_{th}v_{th}A_{PC} \sim \rho v^3 A_{PC}$ where A_{PC} is the polar cap area. In a dipole field a simple consideration shows that $A_{PC} \sim L^{-1} \sim P^{1/6} \sim (\rho v^2)^{1/6}$ and thus $P_{prec} \sim \rho^{7/6}v^{10/3}$.

To summarize, we have obtained that

$$\begin{aligned}
 P_{JH} &\sim \rho^{2/3}v^{4/3} \\
 P_{prec} &\sim \rho^{7/6}v^{10/3} \\
 I &\sim P^{1/3}
 \end{aligned} \tag{9}$$

where ρ and v are the solar wind density and velocity, respectively, $P = \rho v^2$ is the dynamic pressure, and P_{JH} and P_{prec} are the total Joule heating and particle precipitation powers, respectively.

3 Event Descriptions

3.1 April 6-7, 2000 storm

Figure 1 presents the April 6-7 2000 storm observations as well as the storm evolution in two models. Figures 1a-1e show respectively the IMF B_z component, the IMF clock angle, the solar wind dynamic pressure, the AE index computed from 86 stations, and the final Dst index. Figure 1a shows that the IMF B_z turned strongly southward at ~ 18 UT on April 6, 2000, and rotated strongly northward at ~ 00 UT on April 7, 2000. During the storm main phase (18-24 UT) the IMF clock angle was in the sector between 180° and 240° (Figure 1b). The solar wind dynamic pressure (Figure 1c) was unusually high throughout the event, reaching almost 30 nPa during the storm recovery phase at April 7, 2000. The AE index (Figure 1d) was strongly enhanced, being

almost steadily over 1500 nT during the storm. The final Dst index (Figure 1e) decreased close to -300 nT at storm maximum. (For more details, see Huttunen et al., 2002).

Panels 1f and 1g depict the April 2000 storm energetics using two different approaches. The ϵ parameter (Figure 1f) (Akasofu, 1981), which represents the energy input into the inner magnetosphere, enhances to approximately half of its maximum at the SSC and reaches its maximum during the storm main phase. The energy input stops when the IMF B_z turns northward. Panel 1g shows the total energy transferred through the magnetopause as evaluated from the GUMICS-4 global MHD simulation (Palmroth et al., 2003). In the simulation, the energy input also starts at the SSC, but increases immediately to values characteristic of the main phase, and does not decrease to zero when the IMF turns northward. This can be attributed to the fact that the energy input is also dependent on the solar wind dynamic pressure (Scurry and Russell, 1991), a factor that is highly enhanced during the event and is present in the ϵ equation only through the solar wind bulk speed.

3.2 August 15, 2001 substorm

Figure 2 shows the August 15, 2001, substorm observations and the energy transfer rates calculated as above. The solar wind measurements were recorded by the Geotail spacecraft. Panels 2a-2c show the IMF B_z , IMF clock angle, and the solar wind dynamic pressure. The substorm occurred when the North American sector was in the nightside, therefore Panel 2d presents the auroral electrojet index calculated from the CANOPUS magnetometer array. Ten stations (FCHU, CONT, DAWS, ESKI, GILL, ISLL, MCMU, RANK, RABB, FSIM) were used, from which the minimum of the north component was selected at each time step, yielding the CL index. Panels 2e and 2f are the ϵ parameter calculated from the solar wind parameters, and the total energy transferred through the magnetopause surface in the GUMICS-4 MHD simulation using the method described in Palmroth et al. (2003).

Figure 2a shows that the IMF B_z was around zero at the beginning of the simulated time period and turned weakly southward \sim 0339 UT. Simultaneously, the IMF clock angle (Figure 2b) rotated into the sector 120° - 180° . Solar wind dynamic pressure (Figure 2c) was low, below 1 nPa, during the event. The onset of a modest substorm (\sim -500 nT) occurred at 0427 UT in the CANOPUS magnetograms (Figure 2d). Thus, the growth phase of the substorm lasted \sim 48 min, and at substorm onset the IMF was still southward indicating that the energy input mechanism was still active. The ϵ parameter (Figure 2e) started to increase when the IMF B_z turned southward. The ϵ parameter reached a quite moderate peak value of $1 \cdot 10^{11}$ W simultaneously with the minimum of

IMF B_z . The total energy transferred through the MHD magnetopause started to increase about half an hour later than ϵ , and increased until the IMF B_z rotated northward.

As seen from the GUMICS-4 simulation (Pulkkinen et al., 2003, manuscript in preparation), the tail stretched until 5 UT, which was the time of the onset in the simulation. The expansion phase lasted until 0540 UT, and the recovery phase took 25 min. Comparing to Figure 2d, the simulation onset was about half an hour later than the observed onset, and the simulation substorm was half an hour faster than the observed substorm, as they both recovered about the same time

4 Results

4.1 Ionospheric Dissipation

Figures 3a and 3b present respectively the ionospheric Joule heating power and precipitation power in the April 2000 storm. Thick lines show the Joule heating and the precipitation power calculated from the simulation, whereas thin lines depict the Joule heating and the precipitation power using the Ahn et al. (1983) and Østgaard et al. (2002) proxies, respectively. The left vertical axis is for the GUMICS-4 results, whereas the right vertical axis is for the Ahn et al. (1983) and Østgaard et al. (2002) formulas. The Østgaard et al. (2002) method is based on Polar satellite measurements of particle precipitation fitted to AE and AL indices, while Ahn et al. (1983) used an empirical method based on ground magnetic field measurements to calculate the Joule heating rates and fitted the results to AE and AL indices. The Ahn et al. (1983) and Østgaard et al. (2002) proxies are multiplied by two to account for ionospheric dissipation on both hemispheres. Note that the precipitation power computed from the simulation is calculated from 60° latitude poleward, because latitudes below 60° do not reach the $3.7 R_E$ shell (the inner boundary of the magnetospheric domain), and thus there cannot be any magnetospheric precipitation sources below this latitude in the simulation.

As shown in Figure 3, in the simulation at the SSC onset (~ 1640 UT), the precipitation power ($\sim 10 \cdot 10^{10}$ W) slightly exceeds the Joule heating power ($\sim 7 \cdot 10^{10}$ W). After the SSC, the Joule heating power slightly decreases, but the precipitation power stays at the same level. Comparison with Figure 1 shows that the temporal variation of Joule heating resembles the temporal variation of the solar wind dynamic pressure, whereas the precipitation power has a completely different shape. The precipitation power starts to decrease at the end of the storm main phase, while the Joule heating reaches its largest value during the recovery phase during a large peak in the solar wind dynamic pressure. Otherwise, the amount of power dissipated by the precipitation and the

Joule heating are roughly comparable, with precipitation power showing less time variability than the Joule heating power. Table 1 summarises the average and peak values of dissipated Joule heating and precipitation powers, relative contributions are also shown.

In Figure 3a the Joule heating calculated using the Ahn et al. (1983) method does not compare well with the Joule heating calculated from the global MHD simulation. The average level during the storm main phase ($\sim 5 \cdot 10^{11}$ W) is about ten times larger than the Joule heating rate in the simulation. Also the temporal variation of the two curves are different. While the Joule heating in the simulation appears to be correlated with the solar wind dynamic pressure, the Ahn et al. (1983) proxy has (by definition) the shape of the AE index. However, in Figure 3b the precipitation power calculated from the Østgaard et al. (2002) proxy and the precipitation power calculated from the simulation have similar temporal variation, only the precipitation power in the Østgaard et al. (2002) proxy is two times larger than the precipitation power in the simulation. The Østgaard et al. (2002) proxy starts at a higher level before the storm SSC, otherwise the temporal variation of the two curves are remarkably similar.

Figure 4 shows the Joule heating color-coded in the simulation during the April 2000 storm. The units are Wm^{-2} . The pink lines show the potential isocontours with 10 kV spacing. The local noon is at the top, 18 MLT to the left, 24 MLT at the bottom and 6 MLT to the right of each plate. Before the storm SSC (1600 UT) the ionosphere is quiet. At 1800 UT during the main phase, the polar cap potential difference has increased. Also the Joule heating is enhanced, with its maximum clearly on the dayside. Enhanced Joule heating also occurred within the polar cap in the region where the electric field is largest (potential contours are close to each other). Furthermore, there is a faint maximum in the midnight sector along the oval. At 0000 UT, all regions show much enhanced Joule heating power, and the potential difference has further increased. At 0200 UT the Joule heating power has decreased with only a small distribution over the polar cap. At 0300 UT, at the largest peak in the Joule heating power rate during the event (during the largest pressure pulse), the Joule heating power distribution covers both the dayside and the nightside ovals, as well as regions within the polar cap. At 0630 UT, near the end of the simulated period, the decreased Joule heating rate is concentrated within the polar cap; the oval shows only faintly.

Figure 5 shows the precipitation power [Wm^{-2}] color-coded at the same moments of time as in Figure 4. The outermost circle is the latitude 60° in the ionosphere, and the innermost circle is 88° in latitude, and MLT sectors are as in Figure 4. Before the storm (1600 UT) there is no significant precipitation into the ionosphere. At 1800 UT, the precipitation power rate has increased with a clear maximum in the dayside in the cusp region. At 0000 UT the situation has not changed

from the previous panel, but at 0200 UT the dayside maximum has been diminished, and instead particularly in the nightside and dawn oval there are clear precipitation power maxima. At 0300 UT, the precipitation has increased in the oval region, but at 0630 UT the precipitation power rate has decreased almost to the level preceding the storm.

The total ionospheric dissipation can be compared to the total energy transferred through the magnetopause surface (see Figures 1 and 2). As can be seen from Figure 1, the energy input through the magnetopause surface during the main phase of the April 2000 storm is ~ 25000 GW, whereas the ϵ parameter suggests an energy input of ~ 5000 GW during the main phase. The ionosphere consumes the total amount of ~ 190 GW during the main phase, which is less than 1% of the energy transferred through the surface and $\sim 4\%$ of ϵ . During the recovery phase, ~ 10000 GW is transferred through the magnetopause surface, and the total amount of ~ 170 GW, about 2% of input, is dissipated into the ionosphere.

Figure 6 presents the ionospheric Joule heating power and the precipitation power during the August 15, 2001 substorm simulation; the format of the figure is similar to Figure 3. The Joule heating and precipitation powers start to increase around 4 UT reaching their peaks around 0530 UT. The decreasing phase of the ionospheric dissipation lasts until ~ 0620 UT. Both ionospheric dissipation power rates show an increasing trend during the simulated time period. The peak value of the ionospheric Joule heating rate is about 50% of the precipitation energy peak value. Table 2 summarises the ionospheric dissipation power as average and maximum values; also the relative contributions are shown.

For the substorm simulation case, the shapes of the Joule heating and precipitation powers from the Ahn et al. (1983) and the Østgaard et al. (2002) proxies appear to be remarkably similar with the shapes of the Joule heating and the precipitation powers calculated from the simulation. However, note that the scales between the left and right vertical axes are not the same. The Joule heating in the Ahn et al. (1983) proxy is over thirty times larger than the Joule heating in the simulation. The precipitation in the Østgaard et al. (2002) proxy is about ten times larger than the precipitation power in the simulation. Comparing to Figure 2, during the August 15, 2001, substorm, ~ 1200 GW is transferred through the magnetopause surface, while ϵ parameter indicates about 50 GW energy input. The ionosphere consumes only about ~ 14 GW, which is $\sim 1\%$ of the total transferred energy, and $\sim 30\%$ of ϵ .

Figure 7 presents the Joule heating at six instants of time during the August 2001 substorm simulation, the format of the figure is otherwise the same as in Figure 4 but the color scaling is different. Before the substorm onset (0500 UT in the simulation) a small amount of Joule heating

is concentrated mainly in the nightside oval. At 0530 UT, after the onset, the Joule heating power rate is enhanced in the nightside oval, and there is a small maximum in the duskside oval. Half an hour later the Joule heating power is already decreased to the level preceding the substorm.

Figure 8 shows the precipitation color-coded in the simulation during the same time instant as above in Figure 7, and the format of the figure is similar to Figure 5 except for the color scaling. Before the substorm onset there is already a small amount of precipitation centered approximately at the 21 MLT sector, and a smaller maximum exists approximately at the 02 MLT sector. After the onset the precipitation maximum at the 21 MLT sector is enhanced, persisting still at 0600 UT. At 0700 UT the precipitation power has recovered to the level preceding the substorm. The 02 MLT maximum remains approximately the same in size throughout the simulated period.

4.2 Joule Heating Power Distribution in the Ionosphere

Figure 9 presents the ionospheric Joule heating rates distributed at different longitudes and latitudes during the April 2000 storm simulation: Figures 9a-9c show the Joule heating rates in the dayside, dawn and dusk sectors, and in the nightside, respectively. Figures 9d-9f show the Joule heating rates at low latitudes, within the auroral oval, and within the polar cap, respectively. As is evident from Figure 9, the SSC is visible at all local times and latitudes simultaneously around the ionosphere. The temporal variation of the different curves are similar, indicating that all the peaks and valleys in the Joule heating power occur at the same time. However, Figure 9 also shows that the location contributing mostly to the Joule heating rate during the storm evolution is the dayside oval and low latitudes. For instance, the nightside Joule heating rate is about 40% of the dayside Joule heating rate.

Figures 10a-10e present the Joule heating power distribution during the August 15, 2001, substorm simulation in the dayside, dawn and dusk sectors, nightside, low latitudes, oval area, and in the polar cap, respectively. Contrary to the storm event, in the substorm case most of the Joule heating power is concentrated at the oval latitudes. The Joule heating power in the nightside exceeds the Joule heating power in the dawn and dusk and in the dayside.

4.3 Precipitation Power Distribution in the Ionosphere

Figure 11 presents the energy associated with the precipitation in the dayside, dawn and dusk sectors, the nightside (Figures 11a-11c), and in the oval and polar cap areas (Figures 11d-11e) in the April 2000 storm simulation. Figure 11 clearly illustrates that the major part of precipitation power is dissipated in the dayside oval and cusp regions during the April 2000 storm simulation.

Figure 12 shows the precipitation power distributed over latitude and longitude during the August 15, 2001, substorm simulation. Figures 12a-12c show the precipitation powers in the dayside, dawn and dusk sectors, and in the nightside, whereas Figures 12d and 12e depict the precipitation powers in the oval and polar cap areas, plotted in the same scale. Figure 12 demonstrates that during the substorm, a major part of the precipitation power comes from the nightside oval. The dawn and dusk precipitation peak value reaches $\sim 80\%$ of the nightside precipitation peak value.

4.4 Relation between input and output

After calculating the ionospheric dissipation directly from the simulation of the two events, we set out to search for a formulation of the ionospheric dissipation as a function of the solar wind parameters. Ideally one would like to find a general formulation, which gives the same functional dependence on the solar wind parameters for both simulated events, implying that it may be valid also in a more general case. The parameters to be considered include at least the solar wind density ρ , velocity v and the IMF B_z . We chose the simplest power law function for fitting the simulation data, i.e.,

$$P_{ionosphere} = C \left(\frac{\rho}{\rho_0} \right)^a \left(\frac{v}{v_0} \right)^b \left[\exp \left(\frac{B_{z,IMF}}{\sqrt{2\mu_0 p_{dyn}}} \right) \right]^d \quad (10)$$

where $\rho_0 = m_p \cdot 7.3 \cdot 10^6 \text{ m}^{-3} = 1.22 \cdot 10^{-20} \text{ kgm}^{-3}$ and $v_0 = 400 \text{ km/s}$ are chosen as typical solar wind density and velocity, this is for convenience to obtain a correct unit for the power law. C is thus a constant having Watts as units. Because we want to have the power law formula positive and monotonically increasing as a function of negative IMF B_z , we model the IMF B_z inside an exponential. Furthermore, the IMF B_z is scaled in the power law by the magnetopause magnetic field given by the pressure balance equation.

Table 3 shows the fitted coefficients C , a , b , and d , together with their error margins and correlation coefficients with the simulation results. Three fits were made: output $P_{ionosphere}$ taken to be only the Joule heating, only precipitation, and for the sum of Joule heating and precipitation. The first block presents the fitted coefficients, as well as coefficients calculated from the scaling law theory in Section 2.3, for Joule heating power in the two events. Comparison of the fitted and theoretical values indicates clearly that the simulated Joule heating power fitted to the solar wind data gives larger values for a and b in both events compared to what would be expected from the scaling law theory in Section 2.3. In both events, a is roughly the same, but in the April storm simulation b is larger by 1.6 than in the August substorm simulation. This suggests that the

solar wind density has roughly the same influence on the deposited Joule heating power, but in the April storm simulation the solar wind speed has much more influence on the deposited Joule heating power than in the August substorm event. However, the coefficient d should be negative, because the Joule heating rate should increase with increasing negative IMF B_z . As can be seen in Table 3, in the April storm simulation d is positive (but with a large error estimate), and in the August substorm simulation it is negative, indicating that the April storm simulation was more driven by the solar wind dynamic pressure than the IMF direction. Nevertheless, in both events the Joule heating rate calculated using Eq. (10) with the obtained parameters is well-correlated to that given by the simulation; in the April storm event the correlation coefficient is 0.75, whereas in the August substorm simulation the correlation coefficient is 0.83.

The second block of Table 3 presents the results for fitting the solar wind data into the precipitation power calculated in the simulation. The scaling law theory in Section 2.3 now predicts larger a than is obtained by fitting the solar wind data into the precipitation in the simulation. In the August substorm simulation a is comparable in size with a in the April storm simulation. The coefficient b is comparable in size in both events, it is also roughly the same to what the scaling law theory predicts. Curiously, now the coefficient d is negative in the April storm simulation and positive in the August substorm simulation, indicating that the IMF direction would have influence on the deposited precipitation power during the April storm, but during the August substorm the deposited precipitation would be almost independent on the IMF direction. Note however that the error estimate is large for the positive d coefficient in the substorm case. In both events, the precipitation power calculated using Eq. (10) is well-correlated to what is calculated in the simulation, the correlation coefficient being 0.86 for both events.

We further calculated the sum of Joule heating and precipitation powers, and fitted that sum to the solar wind parameters using Eq. (10). The results are presented in the third block of Table 3. Now, a , b , and d are roughly the same for both events, d is negative, the error estimates are small, and the correlation coefficient between the ionospheric dissipation calculated from Eq. (10) and from the simulation is over 0.8. We also merged the two events to one data set, and obtained roughly the same a , b , and d with a correlation coefficient 0.94. All the coefficients are also roughly comparable to the geometric mean of Joule heating and precipitation power scaling exponents. The results are also presented in Figure 13, where the sum of Joule heating and precipitation power is plotted (thick line) with the ionospheric dissipation calculated from Eq. (10) using the solar wind parameters and coefficients given in Table 3 (thin line) for both events separately and for a data vector where the August substorm data is followed by the data from the April storm. Thus, Eq.

(10) can describe the total power consumed by the ionosphere much better than its two contributing pieces (precipitation and Joule heating) separately; also the obtained exponents are closer to the scaling law predictions.

5 Summary and Discussion

In this paper we have calculated the power dissipated into the ionosphere in a global MHD simulation during two events, a magnetic storm and a magnetospheric substorm. We have studied the latitudinal and longitudinal distribution of the ionospheric dissipation from two parameters, the Joule heating and the particle precipitation. Furthermore, we have compared the results to empirical proxies of the Joule heating and precipitation powers. Finally, we have obtained a power law which predicts the total power deposited into the ionosphere from the solar wind parameters with high correlation between the actual simulation results.

Lu et al. (1998) calculated the Joule heating and precipitation powers during a magnetic storm using the AMIE technique. They obtained a globally integrated average of 190 GW for Joule heating, and about 90 GW for particle precipitation during a 2-day storm period in January 1997. Compared to our results in Figure 3 and Table 1, the Joule heating in the MHD simulation consumes less than 100 GW, precipitation about 100 GW in both hemispheres during the storm. Therefore the MHD simulation produces less Joule heating than the AMIE technique, even though the storm modeled in Lu et al. (1998) (D_{st} peak -85 nT) was much smaller than the April 2000 storm. Precipitation in the simulation deposits roughly the same amount of power as that obtained from the AMIE technique. Furthermore, in the Lu et al. (1998) analysis, the peaks in the Joule heating and the precipitation powers are reached at a time when there is a sudden change in the dynamic pressure during the southward IMF period. In the MHD simulation, the peak in the precipitation power occurred during the main phase and southward IMF, also as a response to a solar wind pressure pulse. The peak in the Joule heating power, however, occurs during the largest dynamic pressure pulse, which took place during the storm recovery phase and northward IMF. A closer examination of the simulation results around 3 UT (the time of the maximum Joule heating) reveals that at that time an interhemispherical current system, presumably a result of different conductivities between the two hemispheres, develops into the simulation. Such a current system is likely to cause a large amount of Joule heat, because in an interhemispherical current system the current closes over a large distance from the one hemisphere to another.

The Joule heating power calculated from the MHD simulation is clearly different from the em-

pirical proxy by Ahn et al. (1983) in the April 2000 storm event. The temporal variation of the Joule heating power in the MHD simulation resembles remarkably the temporal variation of the solar wind dynamic pressure, whereas the Joule heating power in the Ahn et al. (1983) formula is a scaled AE index. Janhunen and Koskinen (1997) reported that in the GUMICS-3 MHD simulation (earlier version of GUMICS-4) the Region 1 current system largely closes into the dayside magnetopause currents, which are known to be modified by the solar wind dynamic pressure. Furthermore, the temporal variation of the field-aligned currents in GUMICS-4 (not shown) also resembles the temporal variation of the solar wind dynamic pressure. Therefore it is natural that the Joule heating power, which depends on the square of the field-aligned currents, also follows the solar wind dynamic pressure variations in the GUMICS-4 MHD simulation.

The temporal variation of the calculated precipitation power during both events as well as the temporal variation of Joule heating power during the substorm event is well-correlated with the temporal variation of the empirical proxies of Østgaard et al. (2002) and Ahn et al. (1983). However, the amount of energy deposited into the ionosphere in the simulation is much smaller than the power deposited into the ionosphere in the empirical proxies. The Joule heating power deposited during the storm simulation is 25% of the Joule heating power given by Ahn et al. (1983) formula. The precipitation power deposited into the ionosphere is about 50% of the precipitation power using the Østgaard et al. (2002) formula. The situation is worse in the substorm simulation: The amount of Joule heating power deposited into the ionosphere in the simulation is only 4% of the amount of Joule heating power according to the Ahn et al. (1983) formula. The amount of precipitation power is about 10% of the amount of precipitation power according to the Østgaard et al. (2002) formula.

As the April 2000 storm was so intense that the oval was located further equatorward than is usual, which means that part of the oval was equatorward of the ionospheric mapping of the inner boundary of the GUMICS-4 MHD simulation ($3.7 R_E$). Therefore, a major part of nightside precipitation during the storm is not included in the simulation. On the other hand, also the empirical proxy used in this study (Østgaard et al., 2002) gives the precipitation power using the AL index, which is calculated from magnetometer stations located poleward of the main part of the oval. Thus there are large uncertainties in both the MHD result and in the empirical proxy. In the April 2000 storm case, the amount of power calculated from the Østgaard et al. (2002) proxy is likely underestimated: The peak value of the precipitation power in the Østgaard et al. (2002) proxy is about 400 GW in the major storm of April 2000, and about 150 GW in a moderate localized substorm. A factor of 2-3 increase from a localized substorm to a major storm with the whole

oval filled with auroras appears to be too small. A likely reason for this is that Østgaard et al. (2002) fitted the measured precipitation to the square root of the AL index, which increases too slowly for very large values of energy input. For final comparison of the precipitation powers we will in the future simulate an event where the precipitation power is available directly from UVI measurements onboard the Polar satellite.

Practically all studies concerning the ionospheric dissipation have reached the conclusion that the Joule heating deposits more energy than the precipitation (e.g., Lu et al., 1998). Our result shows the opposite, in both events the precipitation deposits on average slightly more energy than the Joule heating. This can be explained by considering a single current loop that closes through the ionosphere, i.e., a loop where the acceleration region in the magnetosphere and the ionospheric load are connected in series. The power consumed in a current loop is determined by the potential difference and the total current ($P = UI$). In a single current loop the same current flows through the acceleration region and the ionospheric load, and therefore $P_{accel}/U_{accel} = P_{ionosph}/U_{ionosph}$. If we assume that $P_{accel} = P_{prec}$ and $P_{ionosph} = P_{JH}$, we get $P_{prec}/P_{JH} = U_{accel}/U_{iono}$. In both simulated cases $P_{prec}/P_{JH} > 1$, which means that $U_{accel}/U_{iono} > 1$ indicating that the potential difference in the ionosphere is smaller than in the acceleration region, suggesting that the current closes over a relatively short distance in the ionosphere. Therefore, the fact that Joule heating is a smaller energy sink than precipitation in the global MHD simulation indicates that in the simulation the currents close over a short distance in the ionosphere. Satellite observations reported by Marklund et al. (1998) support this behavior: they found that the closure of the field-aligned currents in the ionosphere occurs rather locally, not over the large-scale substorm current wedge as was previously thought.

When comparing the latitudinal and longitudinal distributions of the ionospheric dissipation in the two simulated events the differences between the storm and substorm cases become evident. In short, the dayside has a dominant role in the storm case, whereas the nightside oval dissipates most of the power in the substorm case. Another clear distinction can be seen in the Tables 1 and 2. While in the storm case the Joule heating and the precipitation dissipate roughly the same amount of energy into the ionosphere, during the substorm precipitation energy exceeds that of Joule heating. This can partly be explained by the fact that a large part of the precipitation is not included in the storm simulation, because of the $3.7 R_E$ inner boundary of the magnetospheric domain, which leaves part of the oval equatorward of that boundary.

The final topic of this paper, the development of a simple power law between the solar wind input and the ionospheric output, proved to be a fruitful starting point in using global MHD simu-

lations in investigating the energy transfer and dissipation. We found a remarkably high correlation coefficient for the power law that calculates the total ionospheric dissipation from the solar wind input, using the same exponents for the two events. The power law works best for the sum of Joule heating and precipitation power, which is natural as the two parameters are not independent of each other. The relative importance of the exponents a , b , and d suggests that the solar wind density and velocity have more impact on the total ionospheric dissipation than the IMF B_z . This may not be universally true: Coincidentally, in the two chosen events the impact of the solar wind pressure was stronger than the IMF. In the April 2000 storm the solar wind dynamic pressure was unusually high, and in the moderate August 2001 substorm the IMF B_z was quite weak and not rapidly varying. This suggests that more events with different inputs must be simulated to obtain a power law that would recover the empirically found strong correlation between energy dissipation and IMF B_z .

Acknowledgements. We thank the NSSDC for maintaining the CDAWeb facility through which Geotail data for the simulation input were obtained. The CANOPUS instrument array was constructed and is maintained and operated by the Canadian Space Agency for the Canadian scientific community. The work of M.P. and P.J. is supported by the MaDaMe program of the Academy of Finland.

References

- Akasofu, S. -I., Energy coupling between the solar wind and the magnetosphere, *Space Sci. Rev.* 28, 121-190, 1981.
- Acuña, M. H., Ogilvie, K. W., Baker, D. N., Curtis, S. A., Fairfield, D. H., and Mish, W. H., The global geospace science program and its investigations, *Space Sci. Rev.* 71, 5-21, 1995.
- Ahn, B.-H. J., Akasofu, S. -I., and Kamide, Y., The Joule heat production rate and the particle energy injection rate as function of the geomagnetic indices AE and AL, *J. Geophys. Res.* 88, 6275-6287, 1983.
- Axford, W. I., and Hines, C. O., A unifying theory of high-latitude geophysical phenomena and geomagnetic storms, *Can. J. Phys.* 39, 1433, 1961.
- Dungey, J. W., Interplanetary magnetic field and the auroral zones, *Phys. Rev. Lett.*, 6, 47-48, 1961.
- Huttunen, K. E. J., Koskinen, H. E. J., Pulkkinen, T. I., Pulkkinen, A., Palmroth, M., Reeves, G. D., and Singer, H. J., April 2000 magnetic storm: Solar wind driver and magnetospheric response, *J. Geophys. Res.* 107, doi:10.1029/2001JA009154, 2002.
- Janhunen P., GUMICS-3 - A global ionosphere-magnetosphere coupling simulation with high ionospheric resolution, in *Proc. Environmental Modelling for Space-Based Applications, Sept. 18-20 1996* (ESTEC, The Netherlands, ESA SP-392, 1996).
- Janhunen, P., and H. E. J. Koskinen, The closure of Region-1 field-aligned current in MHD simulation, *Geophys. Re. Lett.*, 24, 1419–1422, 1997
- Janhunen, P., and A. Olsson, The current-voltage relationship revisited: exact and approximate formulas with almost general validity for hot magnetospheric electrons for bi-Maxwellian and kappa distributions, *Ann. Geophysicae*, 16, 292–297, 1998
- Lu, G., Baker, D N., McPherron, R. L., Farrugia, C. J, Lummerzheim, D., Ruohoniemi, J. M., Rich, F. J., Evans, D. S., Lepping, R. P., Brittnacher, M., Li, X., Greenwald, R., Sofko, G., Villain, J., Lester, M., Thayer, J., Moretto, T., Milling, D., Troshichev, O., Zaitzev, A., Odintzov, V., Makarov, G., and Hayashi, K., Global energy deposition during the January 1997 magnetic cloud event, *J. Geophys. Res.*, 103, 11,685–11,694, 1998
- Marklund, G. T., Karlsson, T., Blomberg, L. G., Lindqvist, P.-A., Fälthammar, C.-G., Johnson, M. L., Murphree, J. S., Andersson, L., Eliasson, L., Opgenoorth, H. J., and Zanetti, L. J., Observations of the electric field fine structure associated with the westward traveling surge and large-scale auroral spirals, *J. Geophys. Res.*, 103, 4125-4144, 1998.
- Østgaard, N. R., Vondrak, R., Gjerloev, J. W., and Germany, G. A., A relation between the energy deposition by electron precipitation and geomagnetic indices during substorms, *J. Geophys. Res.*, in press, 2002.
- Palmroth, M., Janhunen, P., Pulkkinen,, T. I. and Peterson, W. K., Cusp and magnetopause locations in global MHD simulation, *J. Geophys. Res.*, 106, 29,435-29,450, 2001.
- Palmroth, M., Pulkkinen, T. I., Janhunen, P., and Wu, C. C., Stormtime energy transfer in global MHD simulation, to appear in the *J. Geophys. Res.*, 2003.

- Papadopoulos, K., Goodrich, C., Wiltberger, M., Lopez, R., and Lyon, J. G., The physics of substorms as revealed by the ISTP, *Phys. Chem. Earth (c)*, 24, 189-202, 1999.
- Pulkkinen, T. I., Ganushkina, N. Yu., Tanskanen, E. I., Lu, G., Baker, D. N., Turner, N. E., Fritz, T. A., Fennell, J. F., and Roeder, J., Energy dissipation during a geomagnetic storm: May 1998, *Adv. Space Res.*, in press 2003.
- Robinson, R. M., Vondrak, R. R., Miller, K., Dabbs, T., and Hardy, D., On calculating ionospheric conductances from the flux and energy of precipitating electrons, *J. Geophys. Res.*, 92, 2565–2569, 1987.
- Scurry, L., and Russell, C. T., Proxy studies of energy transfer to the magnetosphere, *J. Geophys. Res.*, 96, 9541-9548, 1991.
- Turner, N. E., Baker, D. N., Pulkkinen, T. I., Roeder, J. L., Fennell, J. F., and Jordanova, V. K., Energy content in the storm time ring current, *J. Geophys. Res.*, 106, 19,149-19,156, 2001.
- Walker, R. J., Ogino, T., Raeder, J., and Ashour-Abdalla, M., A global magnetohydrodynamic simulation of the magnetosphere when the interplanetary magnetic field is southward: The onset of magnetotail reconnection, *J. Geophys. Res.*, 98, 17,235-17,249, 1993.
- Weiss, L. A., Reiff, P. H., Moses, J. J., Heelis, R. A., and Moore, B. D., Energy dissipation in substorms, in *Proc. of International Conference on Substorms 1, ESA SP-335*, 1992.

Tables

Table 1. Summary of the Power Dissipated Into the Ionosphere During the April 2000 Storm

$[10^{10}W]$	<power>	max(power)
Joule heating	6.9 (42%)	29.1 (57%)
Precipitation	9.5 (58%)	21.8 (43%)

Table 2. Summary of the Power Dissipated Into the Ionosphere During the August 15, 2001, Substorm

$[10^9W]$	<power>	max(power)
Joule heating	3.6 (29%)	6.5 (33%)
Precipitation	8.7 (71%)	12.9 (67%)

Table 3. Power Law Fittings

	C [GW]	a	b	d	corr.	
Scaling law		0.67	1.33			JH
April	4.5 ·(1±0.09)	1.21 ±0.08	3.90 ±0.33	0.57 ±0.38	0.76	JH
August	11 ·(1±0.24)	1.17 ±0.21	2.32 ±0.67	-6.05 ±0.77	0.83	JH
Scaling law		1.17	3.33			Prec.
April	20 ·(1±0.06)	0.36 ±0.05	3.03 ±0.22	-3.31 ±0.25	0.86	Prec.
August	15 ·(1±0.15)	0.68 ±0.13	3.21 ±0.41	0.10 ±0.47	0.86	Prec.
Scaling law*		0.88	2.11			JH+Prec.
April	26 ·(1±0.05)	0.75 ±0.04	2.89 ±0.18	-1.76 ±0.21	0.88	JH+Prec.
August	25 ·(1±0.17)	0.82 ±0.14	3.03 ±0.47	-1.75 ±0.53	0.83	JH+Prec.
Both events	25 ·(1±0.03)	0.80 ±0.03	2.87 ±0.16	-1.81 ±0.18	0.94	JH+Prec.

*Geometric mean of Joule heating and precipitation power scaling exponents.

Figure Captions

Fig. 1. Solar wind conditions during the April 2000 storm. (a) IMF B_z , (b) IMF clock angle, (c) solar wind dynamic pressure, (d) AE index measured at 86 stations, (e) Final Dst index, (f) ϵ calculated from the solar wind parameters, and (g) total energy through the magnetopause surface.

Fig. 2. Solar wind conditions during the August 15, 2001, substorm. (a) IMF B_z , (b) IMF clock angle, (c) solar wind dynamic pressure, (d) CL index calculated from CANOPUS magnetometer network, (e) ϵ , (f) total energy through the magnetopause surface in a global MHD simulation.

Fig. 3. (a) Joule heating power and (b) precipitation power in the ionosphere during the April 2000 storm as described by the GUMICS-4 global MHD simulation (thick line). The thin lines are calculated using equations presented in Ahn et al. (1983) and Østgaard et al. (2002).

Fig. 4. Joule heating power color-coded in the simulation at six moments of time during the April 2000 storm, units Wm^{-2} .

Fig. 5. Precipitation power color-coded in the simulation at six moments of time during the April 2000 storm, units Wm^{-2} .

Fig. 6. (a) Joule heating power and (b) precipitation power in the ionosphere during the August 15 2001 substorm as described by the GUMICS-4 global MHD simulation (thick line). The thin lines are calculated using equations presented in Ahn et al. (1983) and Østgaard et al. (2002).

Fig. 7. Joule heating power color-coded in the simulation at six moments of time during the August 2001 substorm, units Wm^{-2} .

Fig. 8. Precipitation power color-coded in the simulation at six moments of time during the August 2001 substorm, units Wm^{-2} .

Fig. 9. Joule heating power during the April 2000 storm in (a) the dayside 08-16 MLT, (b) dawn 04-08 MLT and dusk 16-20 MLT, (c) nightside 20-04 MLT, (d) low latitudes 0° - 60° , (e) oval latitudes 60° - 75° , (f) polar cap latitudes 75° - 88° . Both hemispheres are present in panels.

Fig. 10. Joule heating power during the August 15, 2001, substorm in the (a) dayside 08-16 MLT, (b) dawn 04-08 MLT and dusk 16-20 MLT, (c) nightside 20-04 MLT, (d) low latitudes 0° - 60° , (e) oval latitudes 60° - 75° , and (f) polar cap latitudes 75° - 88° . Both hemispheres are present in panels.

Fig. 11. Precipitation energy during the April 2000 storm in (a) the dayside 08-16 MLT, (b) dawn 04-08 MLT and dusk 16-20 MLT, (c) nightside 20-04 MLT, (d) oval latitudes 60° - 75° , and (e) polar cap latitudes 75° - 88° . Both hemispheres are present in panels.

Fig. 12. Precipitation power during the August 15, 2001, substorm in the (a) dayside 08-16 MLT, (b) dawn 04-08 MLT and dusk 16-20 MLT, (c) nightside 20-04 MLT, (d) oval latitudes 60° - 75° , and (e) polar cap latitudes 75° - 88° . Both hemispheres are present in panels.

Fig. 13. Sum of Joule heating and precipitation powers (thick line) and fitted curve from Eq. (10) (thin line) for (a) August 15, 2001, substorm simulation, (b) April 6, 2000, storm simulation, and (c) both events merged to the same data vector. Note the different horizontal axis.

Figures

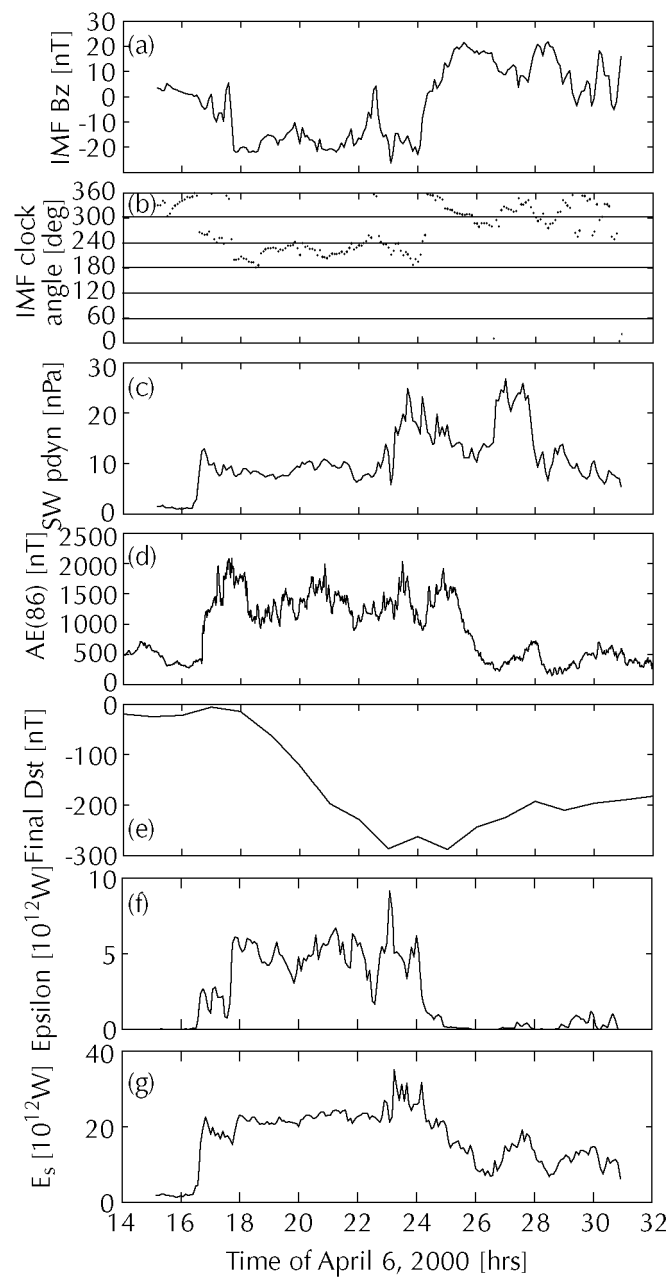


Fig. 1. Solar wind conditions during the April 2000 storm. (a) IMF B_z , (b) IMF clock angle, (c) solar wind dynamic pressure, (d) AE index measured at 86 stations, (e) Final Dst index, (f) ϵ calculated from the solar wind parameters, and (g) total energy through the magnetopause surface.

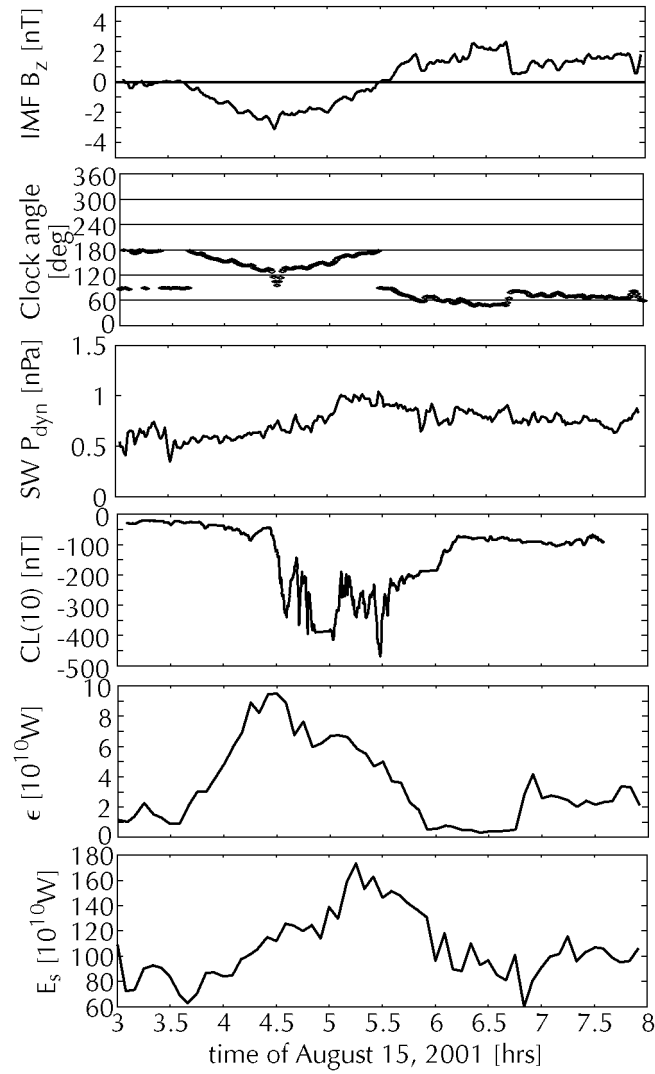


Fig. 2. Solar wind conditions during the August 15, 2001, substorm. (a) IMF B_z , (b) IMF clock angle, (c) solar wind dynamic pressure, (d) CL index calculated from CANOPUS magnetometer network, (e) ϵ , (f) total energy through the magnetopause surface in a global MHD simulation.

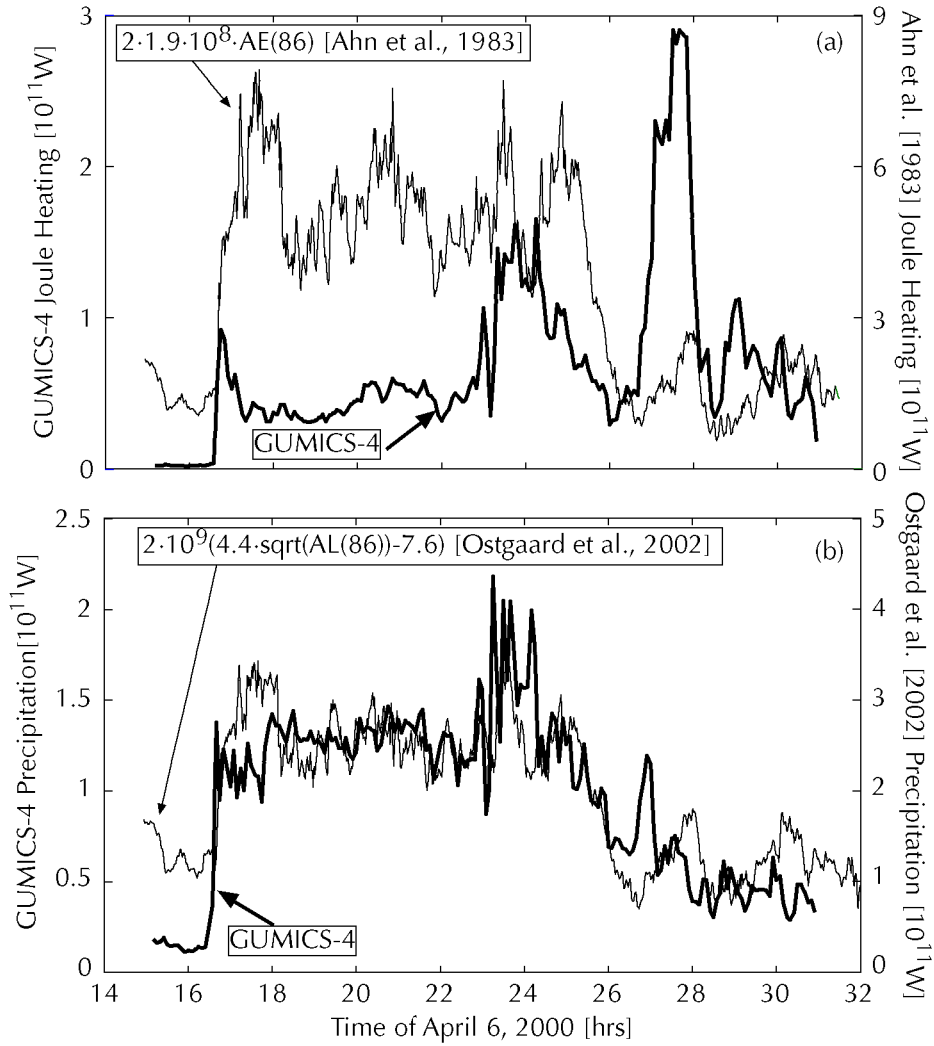
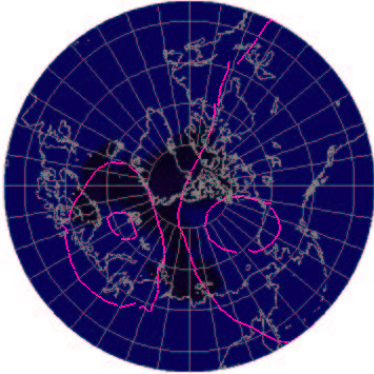
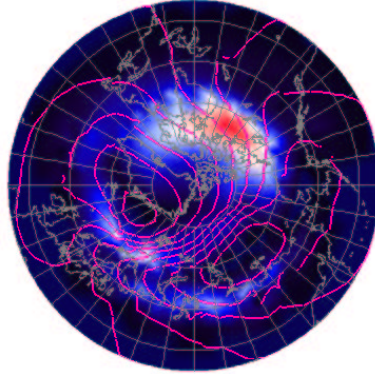


Fig. 3. (a) Joule heating power and (b) precipitation power in the ionosphere during the April 2000 storm as described by the GUMICS-4 global MHD simulation (thick line). The thin lines are calculated using equations presented in Ahn et al. (1983) and Østgaard et al. (2002).

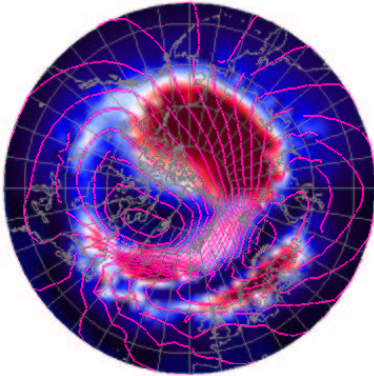
April 6, 1600 UT



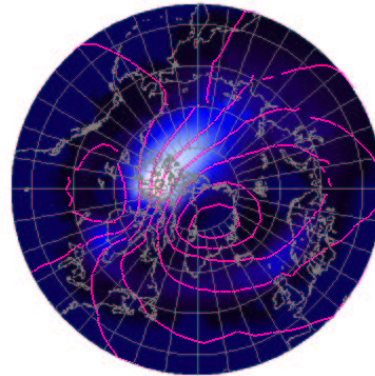
April 6, 1800 UT



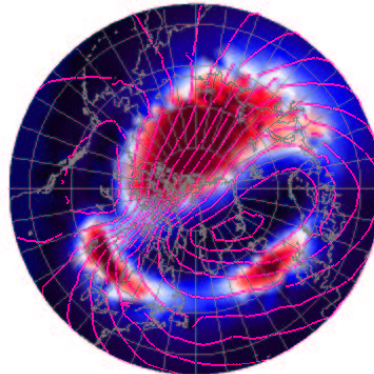
April 7, 0000 UT



April 7, 0200 UT



April 7, 0300 UT



April 7, 0630 UT

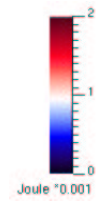
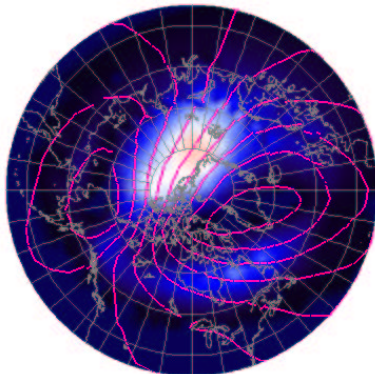


Fig. 4. Joule heating power color-coded in the simulation at six moments of time during the April 2000 storm, units Wm^{-2} .

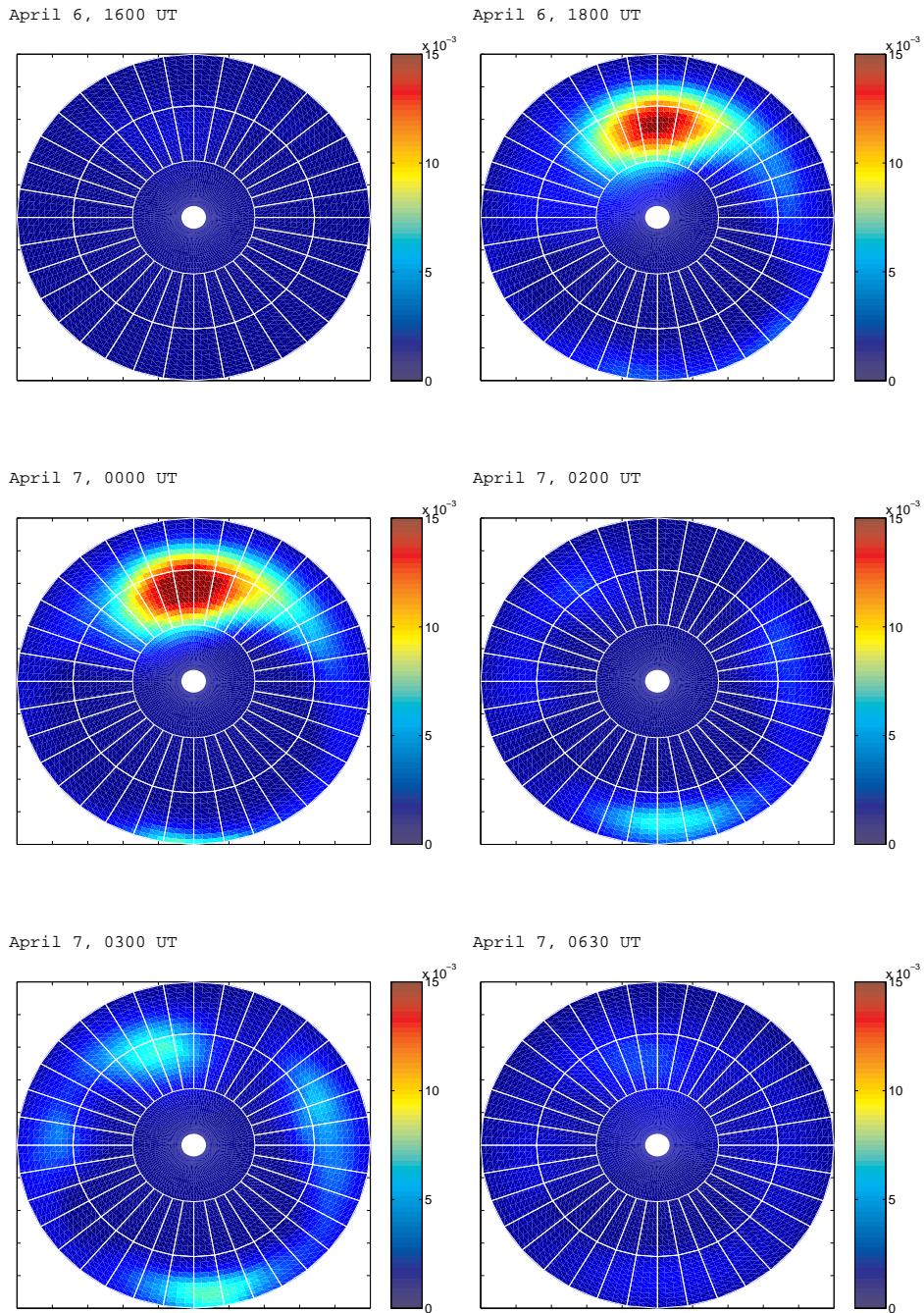


Fig. 5. Precipitation power color-coded in the simulation at six moments of time during the April 2000 storm, units Wm^{-2} .

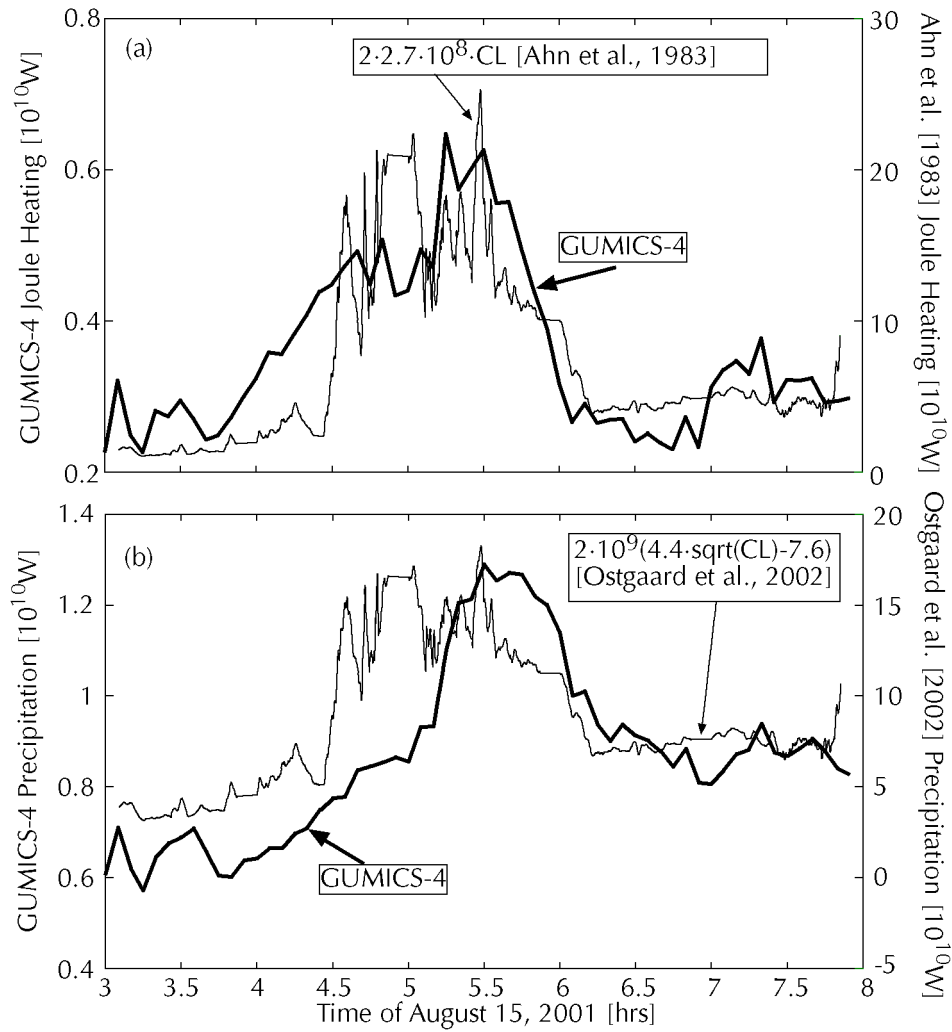
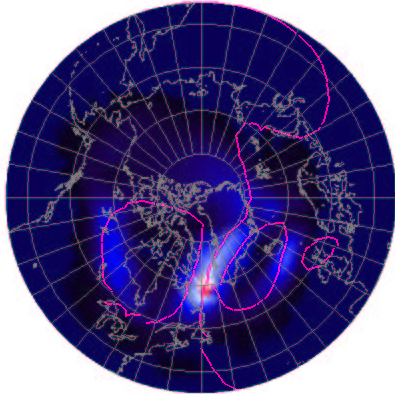
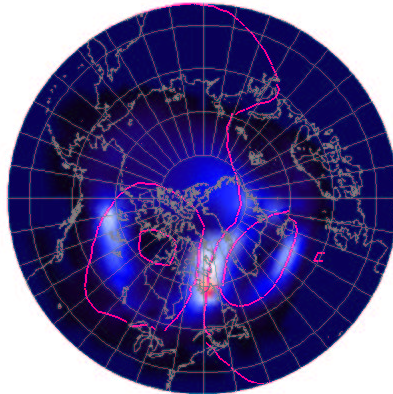


Fig. 6. (a) Joule heating power and (b) precipitation power in the ionosphere during the August 15 2001 substorm as described by the GUMICS-4 global MHD simulation (thick line). The thin lines are calculated using equations presented in Ahn et al. (1983) and Østgaard et al. (2002).

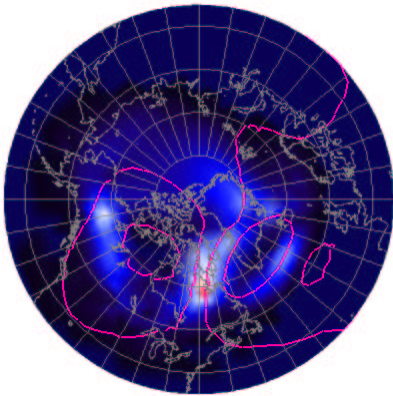
August 15, 0330 UT



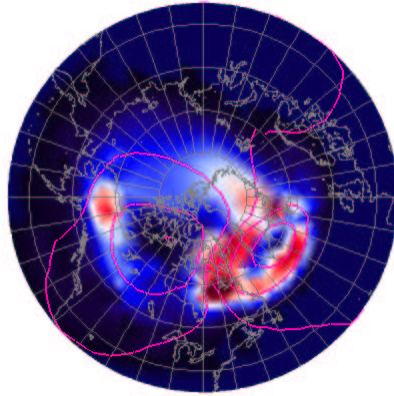
August 15, 0430 UT



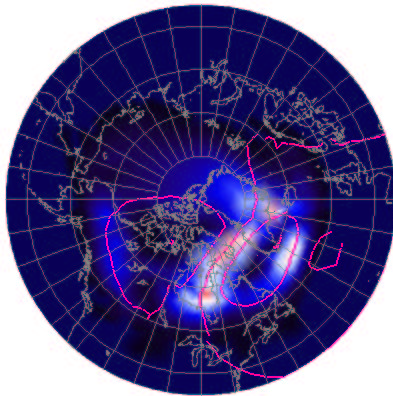
August 15, 0500 UT



August 15, 0530 UT



August 15, 0600 UT



August 15, 0700 UT

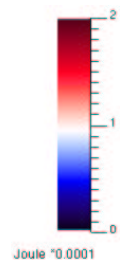
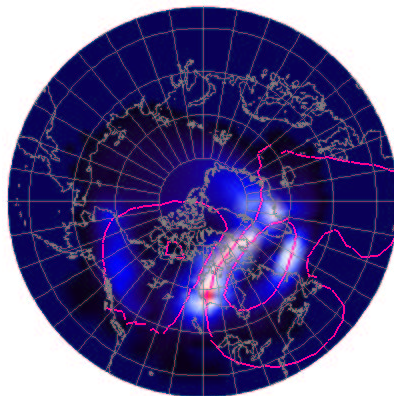


Fig. 7. Joule heating power color-coded in the simulation at six moments of time during the August 2001 substorm, units Wm^{-2} .

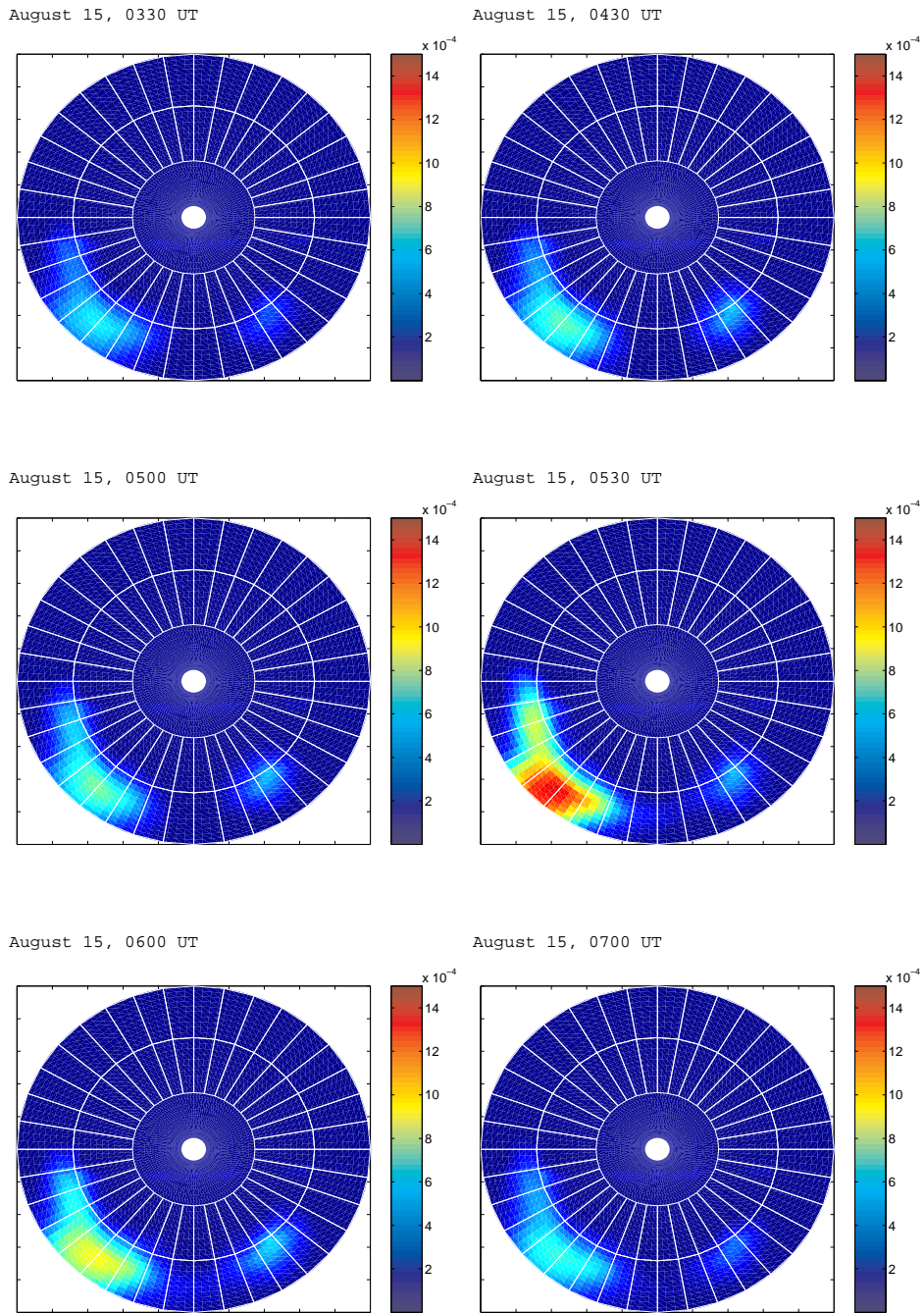


Fig. 8. Precipitation power color-coded in the simulation at six moments of time during the August 2001 substorm, units Wm^{-2} .

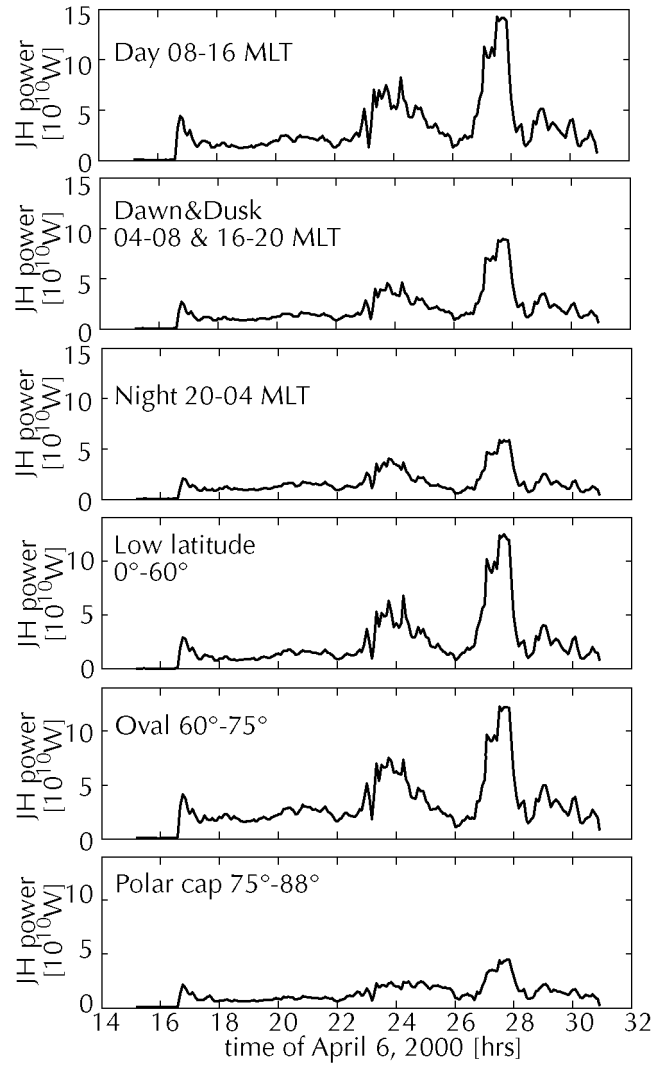


Fig. 9. Joule heating power during the April 2000 storm in (a) the dayside 08-16 MLT, (b) dawn 04-08 MLT and dusk 16-20 MLT, (c) nightside 20-04 MLT, (d) low latitudes 0° - 60° , (e) oval latitudes 60° - 75° , (f) polar cap latitudes 75° - 88° . Both hemispheres are present in panels.

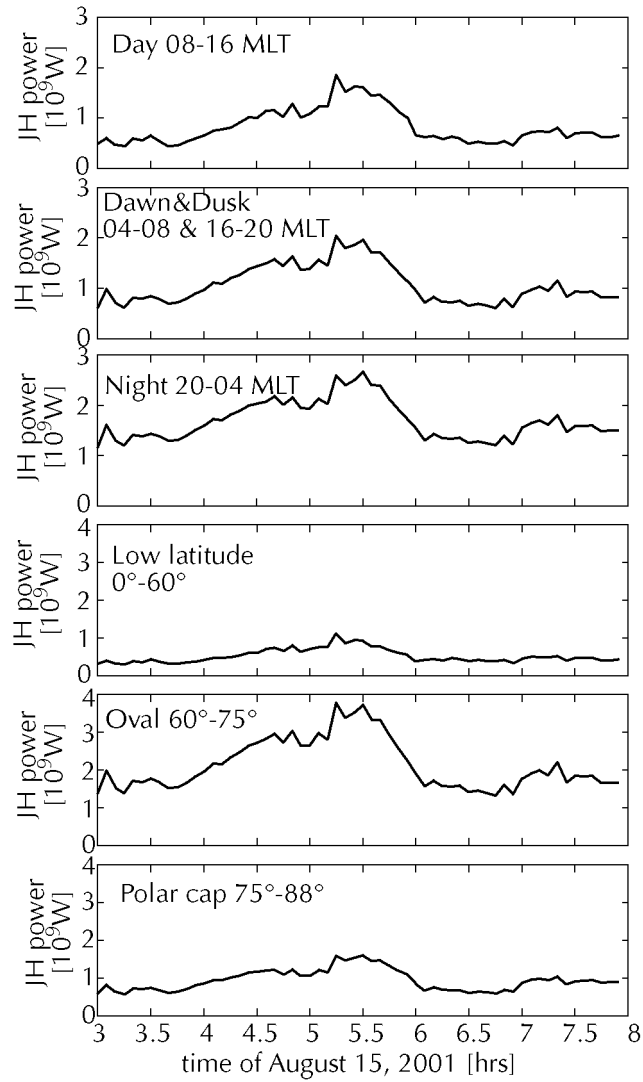


Fig. 10. Joule heating power during the August 15, 2001, substorm in the (a) dayside 08-16 MLT, (b) dawn 04-08 MLT and dusk 16-20 MLT, (c) nightside 20-04 MLT, (d) low latitudes 0° - 60° , (e) oval latitudes 60° - 75° , and (f) polar cap latitudes 75° - 88° . Both hemispheres are present in panels.

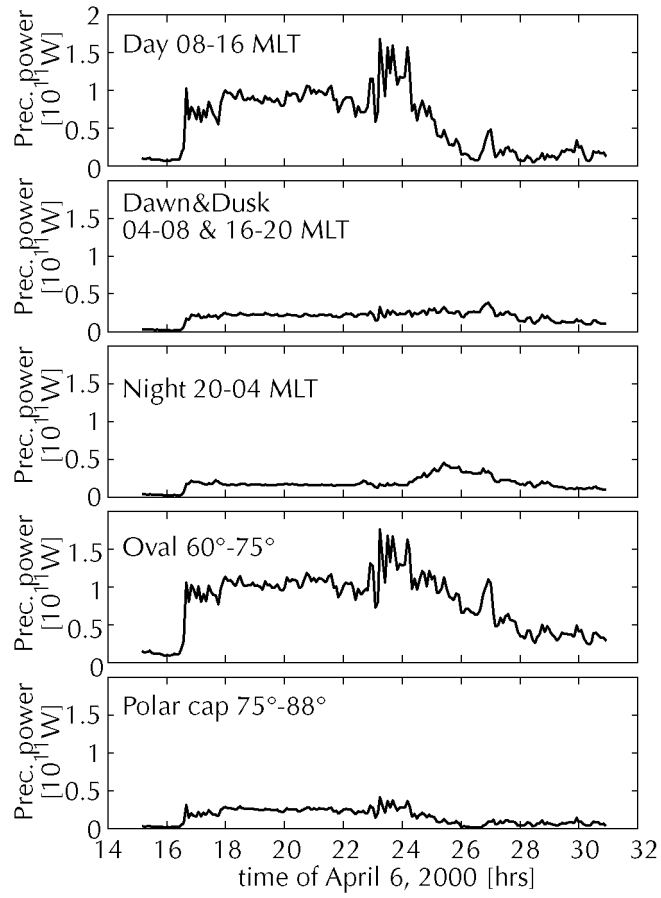


Fig. 11. Precipitation energy during the April 2000 storm in (a) the dayside 08-16 MLT, (b) dawn 04-08 MLT and dusk 16-20 MLT, (c) nightside 20-04 MLT, (d) oval latitudes 60° - 75° , and (e) polar cap latitudes 75° - 88° . Both hemispheres are present in panels.

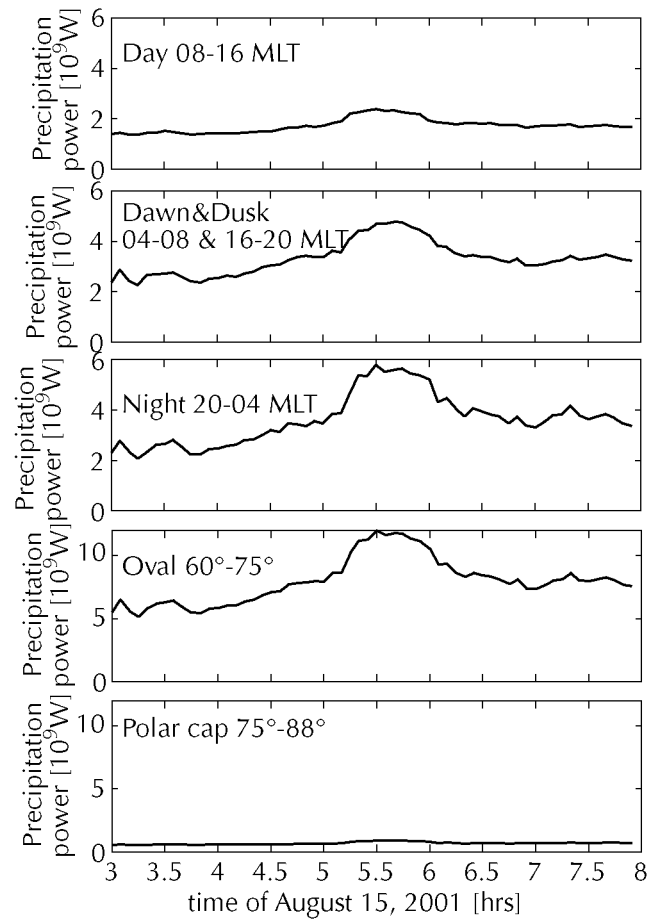


Fig. 12. Precipitation power during the August 15, 2001, substorm in the (a) dayside 08-16 MLT, (b) dawn 04-08 MLT and dusk 16-20 MLT, (c) nightside 20-04 MLT, (d) oval latitudes 60° - 75° , and (e) polar cap latitudes 75° - 88° . Both hemispheres are present in panels.

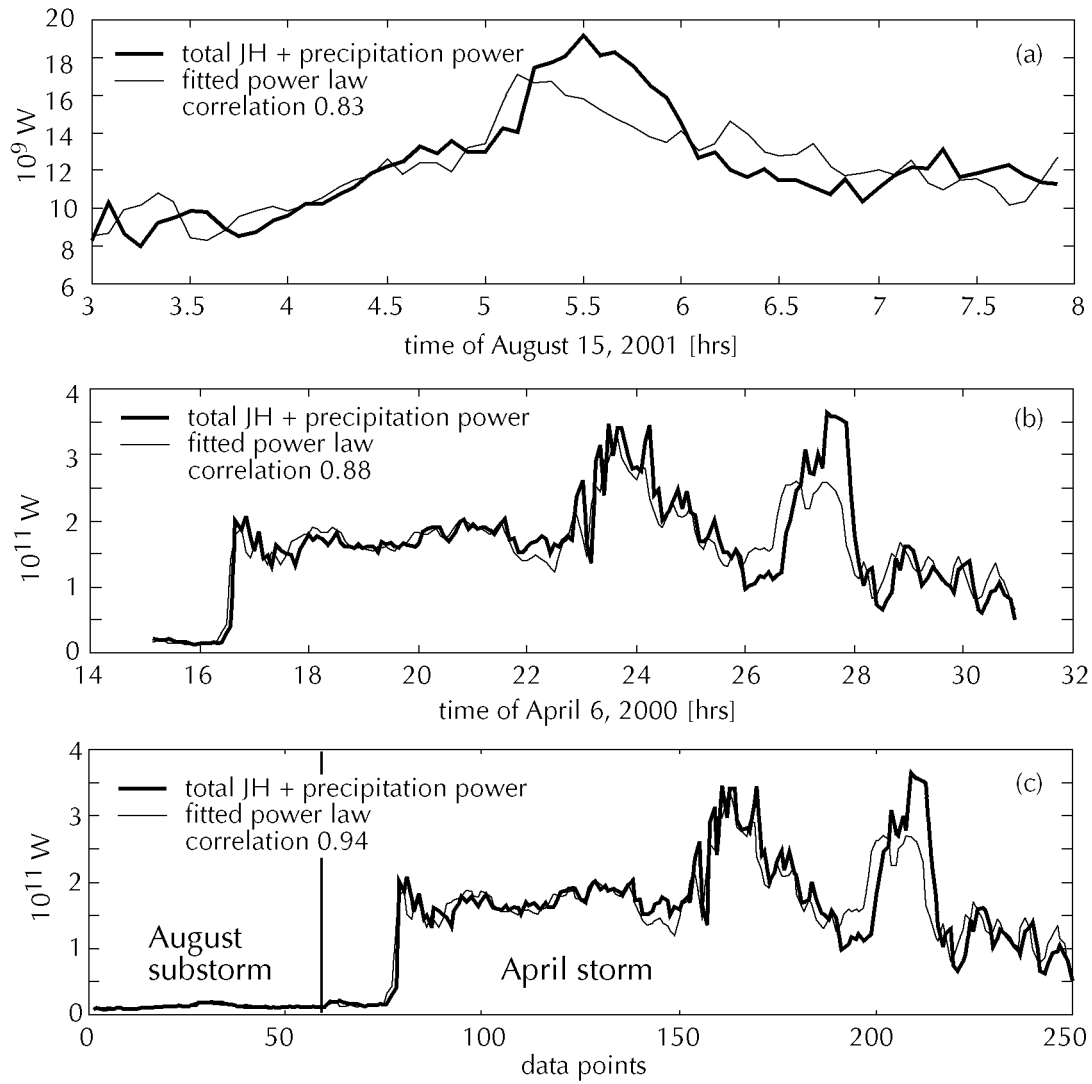


Fig. 13. Sum of Joule heating and precipitation powers (thick line) and fitted curve from Eq. (10) (thin line) for (a) August 15, 2001, substorm simulation, (b) April 6, 2000, storm simulation, and (c) both events merged to the same data vector. Note the different horizontal axis.